A comparative study of microstructure and hydrogen embrittlement of selective laser melted and wrought 17–4 PH stainless steel

Michella Alnajjar, Frédéric Christien, Cédric Bosch, Krzysztof Wolski

To cite this version:

Michella Alnajjar, Frédéric Christien, Cédric Bosch, Krzysztof Wolski. A comparative study of microstructure and hydrogen embrittlement of selective laser melted and wrought 17–4 PH stainless steel. Materials Science and Engineering: A, 2020, 785, pp.139363. 10.1016/j.msea.2020.139363 . emse-03224256

HAL Id: emse-03224256

https://hal-emse.ccsd.cnrs.fr/emse-03224256v1

Submitted on 22 Aug 2022

A comparative study of microstructure and hydrogen embrittlement of selective laser melted and wrought 17-4 PH stainless steel

Michella Alnajjar[a], Frédéric Christien[a], Cédric Bosch[a], Krzysztof Wolski[a]

[a] Mines Saint-Etienne, Univ Lyon, CNRS, UMR 5307 LGF, Centre SMS, F - 42023 Saint-Etienne France

In this study, the microstructure and hydrogen embrittlement of 17-4 PH stainless steel produced by Selective Laser Melting (SLM) were investigated. The microstructure of SLM-ed 17-4 PH stainless steel was found to be fully ferritic, in contrast to the wrought martensitic steel. This finding was correlated to the high cooling and heating rates of the SLM process that suppressed the austenite formation and retained the delta ferrite to room temperature. The SLM-ed steel shows grains elongated in the building direction and its grain size is higher than the prior austenitic grain size of the wrought steel. The two steels present nanoscale copper precipitation after ageing 4 hours at 580°C. The yield strength of the SLM-ed steel was found lower by only 10% with respect to the wrought steel. The hydrogen embrittlement was evaluated by performing slow strain rate tensile tests under cathodic charging after ageing 4 hours at 580°C. It was found that SLM-ed 17-4 PH steel was more susceptible to hydrogen embrittlement compared to its wrought counterpart. This was attributed to the difference in microstructures, more specifically grain size. The crack initiation and propagation was much easier in the ferritic SLM-ed steel than in the martensitic wrought steel because of the higher grain size. The fracture in both steels was due to a significant subcritical crack growth followed by fast overload fracture of the remaining ligament. The fracture surface of the wrought steel showed a brittle intergranular fracture mode close to the surface and a ductile mode at the center. The brittle intergranular fracture mode was associated with the slow subcritical crack growth, while the ductile mode was due to the final fast overload fracture. On the other hand, in the SLM-ed steel, both the subcritical crack growth and the final fast overload fracture were obtained by transgranular cleavage. This shows that under hydrogen the martensitic wrought steel is prone to brittle intergranular fracture in contrast to the ferritic SLM-ed steel which is subject to brittle transgranular cleavage. The same tendency is obtained under air when notched specimens are used. This propensity of the martensitic steel to fracture along prior austenite grain boundaries can be interpreted in terms of the easiest fracture path.

Introduction

Precipitation hardenable stainless steels are widely used in a variety of applications such as chemical plants, oil and gas industry and marine environment due to their combined high strength and good corrosion resistance [1]. 17-4 PH is a precipitation hardenable stainless steel that contains 15-17.5 wt.% of chromium, 3-5 wt.% of nickel and 3-5 wt.% of copper. This steel exhibits a martensitic microstructure after a solution heat treatment and quenching. A subsequent aging treatment is usually applied in the temperature range 480-620°C, which results in strengthening due to the precipitation of copper rich particles in the martensitic matrix [2–5]. 17-4 PH is the most popular grade among the precipitation hardenable stainless steels because it possesses a relatively high tensile strength, fracture toughness and corrosion resistance. However it can be susceptible to hydrogen embrittlement [6–9]. Chiang *et al.* [6] found that the solution treated steel had better resistance to hydrogen embrittlement than the peak aged steel. This was attributed to copper precipitation in the latter that induced its brittle fracture. In contrast, Hayashi *et al.* [7] showed that solution treated and sub-aged steels were more susceptible than peak-aged and over-aged steels to hydrogen embrittlement under low hydrogen content. In that study, the copper precipitation had a beneficial effect by hydrogen trapping. However, this effect disappeared when the hydrogen was trapped both at the precipitates and the martensitic matrix. Shen *et al.* [8] studied the effect of solution treatment temperature on hydrogen susceptibility of 17-4 PH steel. They found that susceptibility decreases and then increases as the solution-treatment temperature increased. This behavior was due to the combined effect of prior austenitic grain size and the state of copper precipitation. Based on these findings, the copper effect on hydrogen susceptibility of this steel is still unclear and needs more investigation. Furthermore, the strength level might have an effect but was not considered in those studies. Murray *et al.* [9] investigated the hydrogen embrittlement of a precipitation hardenable stainless steel similar to 17-4 PH steel and found that the hydrogen susceptibility increased with the increase in strength. For all these studies, the hydrogen embrittlement was evaluated by a loss in ductility and reduction of fracture stress. In addition, fracture surfaces changed from ductile mode for the hydrogen free specimens to brittle mode, such as quasi-cleavage or intergranular fracture, for the hydrogen charged specimens.

Recently, stainless steels have been produced by additive manufacturing (AM). This process has been gaining increased attention because it allows objects, usually having a complex geometry, to be directly fabricated layer by layer according to a computer-aided design (CAD) model [10,11]. Selective Laser Melting (SLM) is a technique of AM that consists of producing metallic components by laser melting of metallic powders [12–14]. Many researches have been conducted on the microstructure of stainless steels obtained by SLM. They have shown that their microstructures can be highly anisotropic and in some cases can have different phase constitution from their wrought counterparts [15–19]. Consequently, the degradation properties of AM stainless steels, in particular their hydrogen embrittlement susceptibility, are expected to be different from their wrought counterparts.

Very few studies have been dedicated to the hydrogen embrittlement of steels obtained from AM. Li et al. [20] showed that a SLM-ed 300 maraging steel was sensible to hydrogen embrittlement. They suggested that embrittlement could be due to the transformation of retained austenite to martensite during mechanical loading under hydrogen. However no comparison with the conventional 300 maraging steel was proposed in their study. Kwon et al. [21] compared the hydrogen embrittlement susceptibility of 18Ni 300 maraging steel in the as-built SLM state and the solution-treated state, with and without ageing treatments. In the aged state, the two materials (SLM-ed as-built and solution-treated) show similar high sensibility, whereas in the non-aged state, the SLM-ed as-built material was found more sensible than its solution-treated counterpart. The authors analysed the behavior of the H-charged materials in terms of hydrogen-microstructure interactions and suggested a detrimental effect of the high austenite content and high dislocation density in the SLM material. However the possible effect of microstructure differences between the two materials on crack initiation and propagation was not discussed. In a review paper, Ornek [22] suggested that possible large grains resulting from AM could affect the resistance to hydrogen embrittlement, but the supporting literature [23] cited by Ornek dealt with conventional wrought materials, not AM ones.

The degradation properties of AM stainless steels need to be investigated in order to prevent the failure of components during service. In this study, the microstructure and hydrogen embrittlement susceptibility of a 17-4 PH stainless steel produced by SLM were investigated. The same ageing treatment was conducted on the two steels, which resulted in similar yield strength. Tensile tests were performed on hydrogen charged and uncharged specimens. Furthermore, the effect of displacement rate and H pre-charging on the hydrogen embrittlement was investigated. The study was conducted in a comparative manner using the wrought steel as a reference.

Experimental procedures

Material

The materials used in this study were wrought and SLM-ed 17-4 PH steels. The wrought material was a commercial bar from UGINE (cast # 818025). It was studied after a solution heat treatment at 1050°C for 1 hour followed by a water quench, then aged at 580°C for 4 hours. The SLM-ed steel were fabricated in an SLM machine of type EOS M270. The fabrication was done in an argon purging environment. Cylinders 100 mm in length, 15 mm in diameter, were fabricated horizontally, i.e. with their axis perpendicular to building direction Z. Tensile specimens were machined from the cylinders and then aged at 580°C for 4 hours. The chemical composition of both materials is given in Table 1. The full composition of the wrought material is indicated (data from the steel provider) in the first line of Table 1. Additional measurements were conducted on both wrought and SLM-ed materials (lines 2 and 3 of Table 1). These measurements were carried out using X-Ray Fluorescence (XRF) (FISCHERSCOPE X-Ray XAN-FD) for elements Ni, Cr and Cu, and using Combustion Elemental Analysis (CEA) for C, S (LECO CS 444/LS), N and O (LECO TC-436).

Table 1: Chemical composition (wt. %) of wrought and SLM-ed 17-4 PH stainless steels

17-4 PH		C	Ni	Si	P	Mn	Cr	Cu	S	N	O	Nb	Fe
Wrought	Provider Data sheet	0.031	4.82	0.31	0.016	0.81	15.61	3.12	0.02	-	-	0.21	Bal.
	XRF/CEA	0.026	4.95	-	-	-	16.18	3.09	0.021	0.033	0.007	-	Bal.
SLM-ed	XRF/CEA	0.03	4.16	-	0.008	-	16.11	3.73	0.003	0.033	0.046	0.3	Bal.

Microstructural characterization

Samples were polished up to 1200 grit, followed by electropolishing using 94% ethanol + 6% perchloric acid as electrolyte at 25 V for 60 s. Scanning electron microscope Zeiss SUPRA55VP was used at 20 kV for Electron Backscatter Diffraction (EBSD) and at 5 kV for imaging and Energy Dispersive X-ray Spectroscopy (EDS). Before conducting high resolution EDS mapping, the electron beam was stabilized for 12 hours in the conditions of acquisition, and the acquisition time of the map was limited to 2 hours to keep the beam drift as low as possible. EBSD data were processed using the MTEX software package [24] working under Matlab so as to extract the phase maps, orientation maps (Inverse Pole Figure, IPF) and grain size distribution. From the EBSD data obtained on martensite, the parent austenite microstructure was reconstructed using the algorithm developed by Nyyssönen et al. [25], which can be used in the MTEX/Matlab environment. This algorithm determines whether some neighboring grains, based on their orientation, share the same prior austenitic grain orientation or not. The Kurdjumov-Sachs relationships [26] are used as a first estimation of the martensite/austenite orientation relationships (OR). However the actual OR are iteratively determined by the algorithm and can slightly differ from Kurdjumov-Sachs. The nature of different boundaries present in the martensitic microstructure (block boundaries, packet boundaries and former austenitic grain boundaries [27]) can also be extracted from the reconstruction procedure.

Tensile tests in air

Only aged materials (4h at 580°C) were tensile tested in air. Two specimen geometries were used: smooth axisymmetric specimens with a gage length of 10 mm and a diameter of 5 mm and notched axisymmetric specimens with a 1 mm deep circumferential notch having a root radius of 0.4 mm and an angle of 35°, which was cut at the center of the gage length. The notched specimens were used in order to study the effect of the notch on the fracture mode in air. Both smooth and notched specimens were tested at room temperature. The displacement rate used during testing was 10^{-5} mm/s.

Tensile tests under cathodic charging

Only aged materials (4h at 580°C) were tensile tested under cathodic charging. All the tensile tests under cathodic charging were conducted at room temperature on smooth specimens. Some specimens were hydrogen pre-charged for 24 hours before the slow strain rate tensile test was started. Then, the hydrogen charging was maintained during the tensile test until specimen fracture. These specimens will be denoted as “pre+charged” specimens. Other specimens were only charged during the slow strain rate tensile tests until fracture (without any pre-charging) and will be denoted as “charged” specimens. All specimens were cathodically charged at -800 mV versus the Saturated Calomel Electrode (SCE) using a PGP201 potentiostat. The charging was done in (30 g/l NaCl + 0.4 g/l sodium acetate) solution at pH 1.5. The solution was deaerated continuously by a nitrogen flux. A platinum plate was used as a counter electrode. The specimens were polished up to 1 µm diamond finish. They were rinsed with water and cleaned with ethanol before each test. The specimen was then installed in the electrochemical cell on the tensile machine. The cell was purged for 10 min with nitrogen gas before introducing the solution. Once the three electrodes were immersed, the cathodic potential was directly applied. The displacement rates applied were 10^{-6} mm/s, 10^{-5} mm/s and 10^{-4} mm/s. The tensile machine used for both charged and uncharged specimens was of type SCHENCK coupled with the Wavematrix software. The recorded parameters are the load and the displacement using linear variable differential transformer (LVDT) sensor. Since the LVDT sensor was placed outside the electrochemical cell, a correction of the raw data was applied so as to obtain the correct deformation in the elastic domain. After the

SSRT test was finished, the specimen was unmounted and cleaned with ethanol. The fracture surface was then examined by scanning electron microscopy.

Electrochemical permeation test

Electrochemical permeation was used to investigate the hydrogen diffusion in the studied materials. The method used is that developed by Devanathan and Stachurski [28]. The specimen was cathodically charged by applying a potential of -1200 mV/SCE on the entry side to maintain a constant hydrogen concentration. The potential applied on the exit side was 0 mV/SCE, which allowed complete oxidation of hydrogen, resulting in a constant zero hydrogen concentration on the exit side. The equipment used for applying the required potentials were PGP201 potentiostats. The solution used in both entry and exit cells was 0.1 M NaOH continuously deaerated with nitrogen. The permeation tests were performed at room temperature. Platinum auxiliary electrodes and SCE reference electrodes were used. The working electrode was a thin sample of the tested steels. The two sides of the sample were polished down to 0.25 µm diamond finish. After preparation, the obtained thickness was between 200 and 400 µm. The sample was then placed and sealed between the two electrochemical cells. A circular area of 0.785 cm^2 (1 cm in diameter) was exposed to the solution on both sides.

The effective hydrogen diffusivity, D_{eff} (m^2/s), was estimated by the time lag method applied on the rising permeation current transient [28]:

$$D_{eff} = \frac{e^2}{6t_L} \qquad 1)$$

where e is the specimen thickness and t_L is the time lag corresponding to the point on the hydrogen permeation curve where the current density at the exit side I is equal to 0.63 I_{ss}, I_{ss} being the steady-state current density. The permeation curves presented in this paper represent the normalized intensity (I/I_{ss}) on the exit side versus the normalized time (t/e^2).

Results and discussion

Microstructural analysis

Figure 1a shows the EBSD phase map of the wrought 17-4 PH steel (1h at 1050°C + 4h at 580°C) obtained from EBSD. Two phases are identified with body centered cubic (BCC) and face centered cubic (FCC) structures respectively. The BCC and FCC contents are 90.5% and 5.2% respectively, the rest not being indexed. It should be reminded here that martensite in this steel has a BCC crystal structure, not BCT (body centered tetragonal), because of the low carbon content [29] [30]. Figure 1b shows the EBSD orientation map of the BCC phase (IPF Z, Z being defined here as the rolling direction of the bar). A well-defined martensitic microstructure is observed with lathes of martensite gathered into blocks and the latter into packets inside prior austenitic grains. The martensitic transformation of 17-4PH steel has already been documented in literature. It takes place upon cooling from the austenitic domain between 130°C and room temperature [30] [31]. Figure 1d shows the orientation map of the parent austenitic microstructure obtained from the reconstruction algorithm. From the reconstruction procedure, it is also possible to identify the block and packet boundaries inside the former austenitic grains. Figure 1c shows the different types of boundaries of the martensitic microstructure. The 5% of FCC phase observed correspond to the sum of retained austenite (untransformed austenite during quenching) and reverted austenite that has possibly formed during ageing at 580°C.

Figure 2a and Figure 2c show the EBSD phase maps of the SLM-ed 17-4 PH steel in the (X-Z) and (X-Y) planes respectively. The (X-Z) and (X-Y) planes are respectively the planes parallel and perpendicular to the building direction Z. On average the BCC and FCC contents are 95.5% and 1.5% respectively, the rest not being indexed. Figure 2b and Figure 2d show the orientation maps of the BCC phase (IPF Z, Z being defined here as the SLM building direction). They reveal a microstructure very different from the wrought steel. A relatively coarse grain microstructure is observed and the usual aspect of the martensite microstructure (prior austenite grains divided in packets, packets divided in blocks) is not evidenced. The reconstruction algorithm, when used for this microstructure, fails in finding any possible common parent austenitic orientation for any group of neighboring BCC grains. This shows, from a crystallography point of view, that the microstructure of the SLM-ed material is not martensitic. It has been shown in a previous paper [15] that this SLM-ed steel in the as-built state has a ferritic microstructure, more specifically δ ferrite. This is due to the high heating and cooling rates

(~ 10^5 to 10^6 K/s) experienced during SLM construction that suppress the transformation of δ ferrite to austenite at high temperature. Thus, the δ ferrite formed during solidification does not undergo any metallurgical transformation during the numerous heating and cooling stages of the construction. This process can be visualized as if δ ferrite had by-passed the austenite phase. As a result, the δ ferrite is retained until the end of the fabrication. In other words, the microstructure obtained is the δ-ferritic solidification microstructure. More details of this by-passing phenomenon are given in [15]. This mechanism has also been recently observed by several research groups on SLM-ed 17-4PH steel [32] [33]. The EBSD maps also show that the grain morphology is different in the (X-Z) plane (Figure 2b) and the (X-Y) plane (Figure 2d), which is related to the SLM process [19,34]. This difference in grain morphology between the planes might play a role in the hydrogen diffusion during tensile tests under hydrogen charging and will be discussed later.

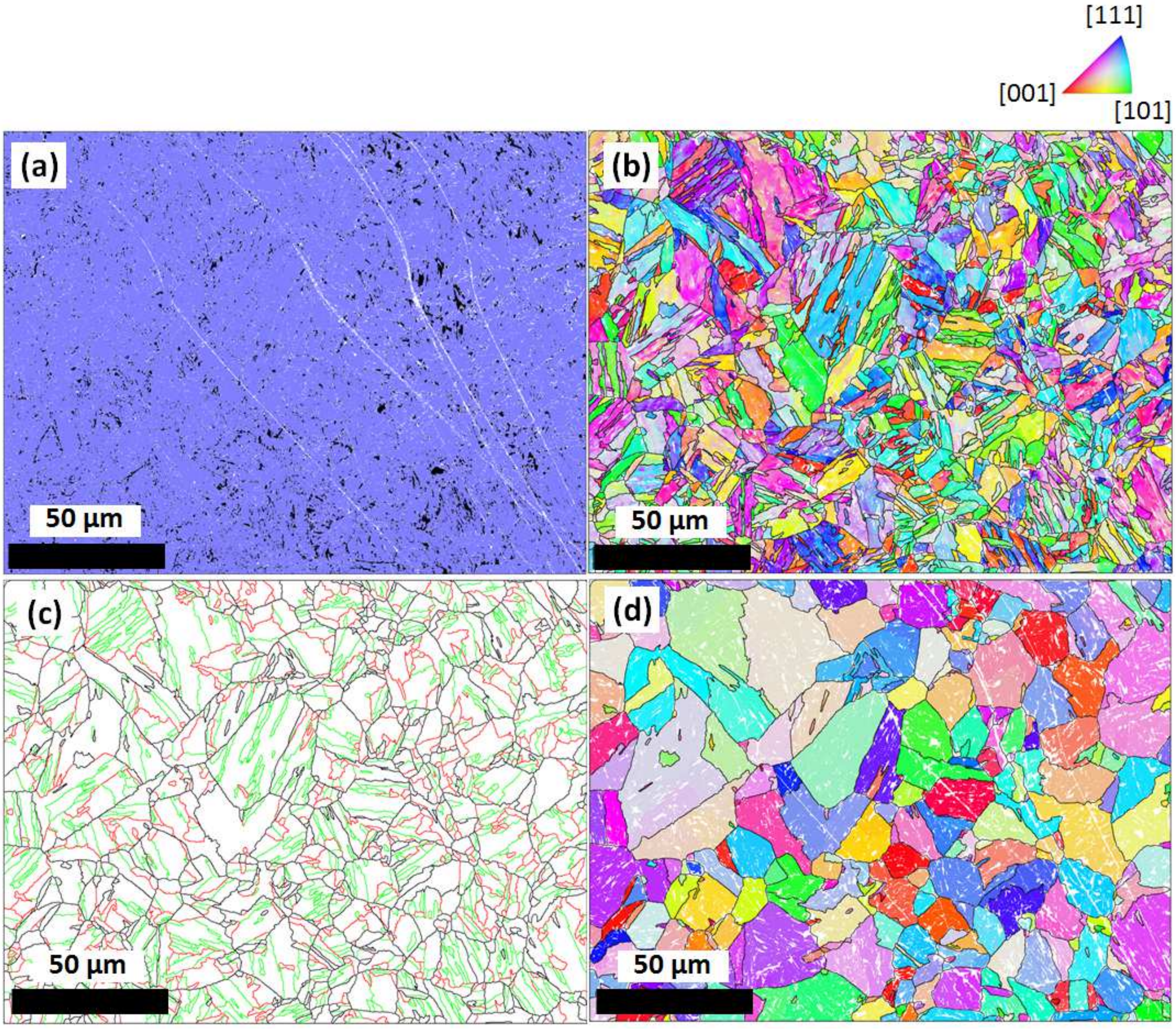

Figure 1: EBSD data obtained on the wrought 17-4PH steel aged 4 hours at 580°C. (a): phase map. The BCC and FCC phases are in blue and black respectively. The non-indexed areas are in white. (b): orientation map (IPF Z, where Z is the rolling direction of the bar), (c): orientation map of the parent austenite microstructure obtained from the reconstruction algorithm. (d): the different types of grain boundaries obtained from the parent austenite reconstruction: prior austenite grain boundaries in black, packet boundaries in red and block boundaries in green.

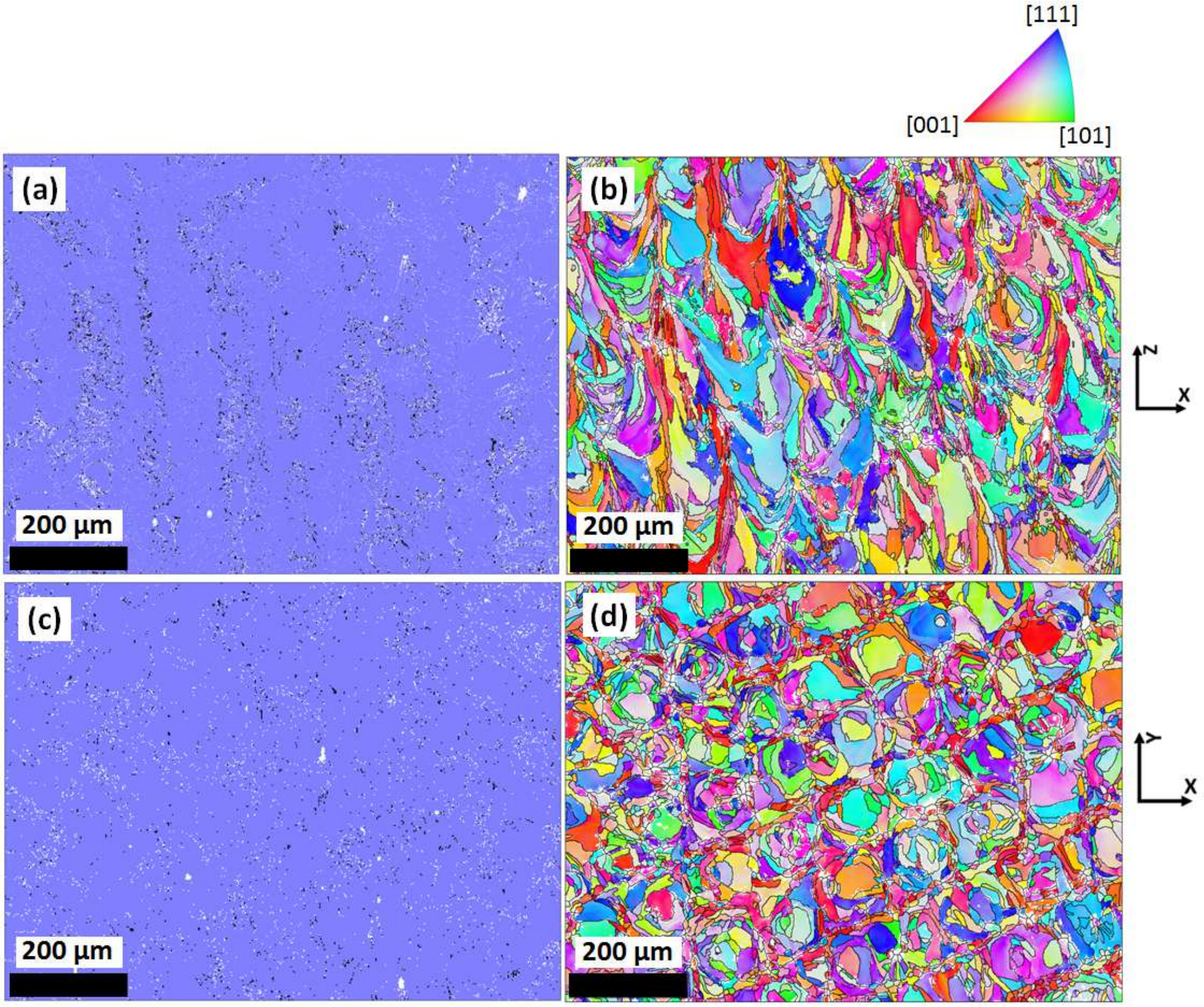

Figure 2: EBSD data obtained on the SLM-ed 17-4PH steel aged 4 hours at 580°C. (a): phase map of the X-Z plane. The BCC and FCC phases are in blue and black respectively. The non-indexed areas are in white. (b): orientation map of the X-Z plane (IPF Z, where Z is the building direction), (c): phase map of the X-Y plane. (d): orientation map of the X-Y plane

Figure 3 shows the grain size distributions determined from EBSD for the two materials. The grain size is defined here as the average equivalent diameter of the grains identified from EBSD. The mean grain sizes <d> are also summarized in Figure 3. Figure 3a gives the martensitic block size distribution, obtained from the EBSD map shown in Figure 1b. This distribution is obtained considering any type of boundary (block, packet or prior austenitic grain boundaries). A mean martensitic block size of 3.0 µm is obtained. Figure 3b shows the former austenitic grain size distribution, determined after parent grain reconstruction (Figure 1d). Only prior austenitic grain boundaries are considered here. A mean prior austenitic grain size of 9.1 µm is obtained. Figure 3c presents the ferritic grain size distribution of the SLM-ed material. It was obtained by averaging the two distributions corresponding to planes (X-Z) and (X-Y) (Figure 2b and Figure 2d respectively). A mean ferritic grain size of 20.4 µm is obtained. The SLM-ed steel shows much larger grains than the wrought steel. In addition, the distribution is very broad: the biggest grains have a diameter as large as 100 µm.

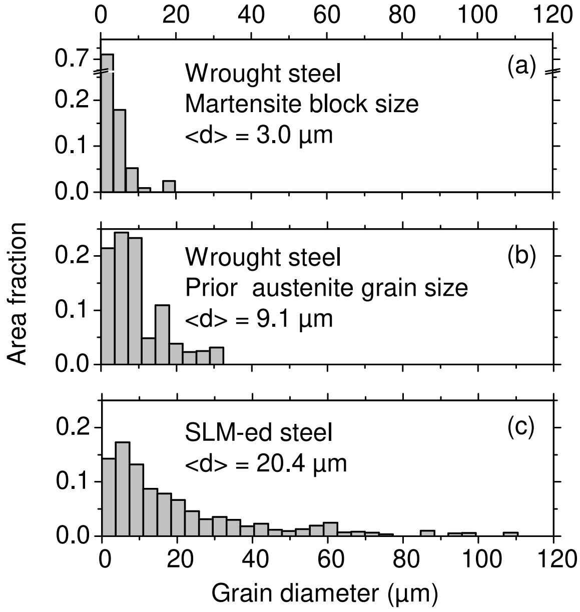

Figure 3: Grain size distributions determined from EBSD. (a): Martensite block size of the wrought 17-4PH steel. (b): Prior austenitic grain size of the wrought 17-4PH steel. (c) Ferritic grain size of the SLM-ed 17-4PH steel. The two materials were aged 4 hours at 580°C.

High resolution SEM observations of the two materials after 4 hours of ageing at 580°C are presented in Figure 4a and Figure 4b. Both materials present some black and white dots. Their size (some nanometers or tens of nanometers) is consistent with the copper precipitation taking place in the 17-4PH steel after ageing at that temperature [5] [35]. It is reasonable to assume that the white dots observed correspond to copper precipitates shallowly buried below the surface, while the black dots correspond to holes due to the dissolution of surface copper precipitates during electropolishing. The 5 kV EDX maps presented in Figure 5 confirm the copper nanoscale precipitation after ageing 4 hours at 580°C in the two materials (wrought and SLM-ed). Additional SEM observations and EDX mapping were conducted on the wrought material in the quenched state as a control material without copper precipitation (Figure 4c and Figure 5c).

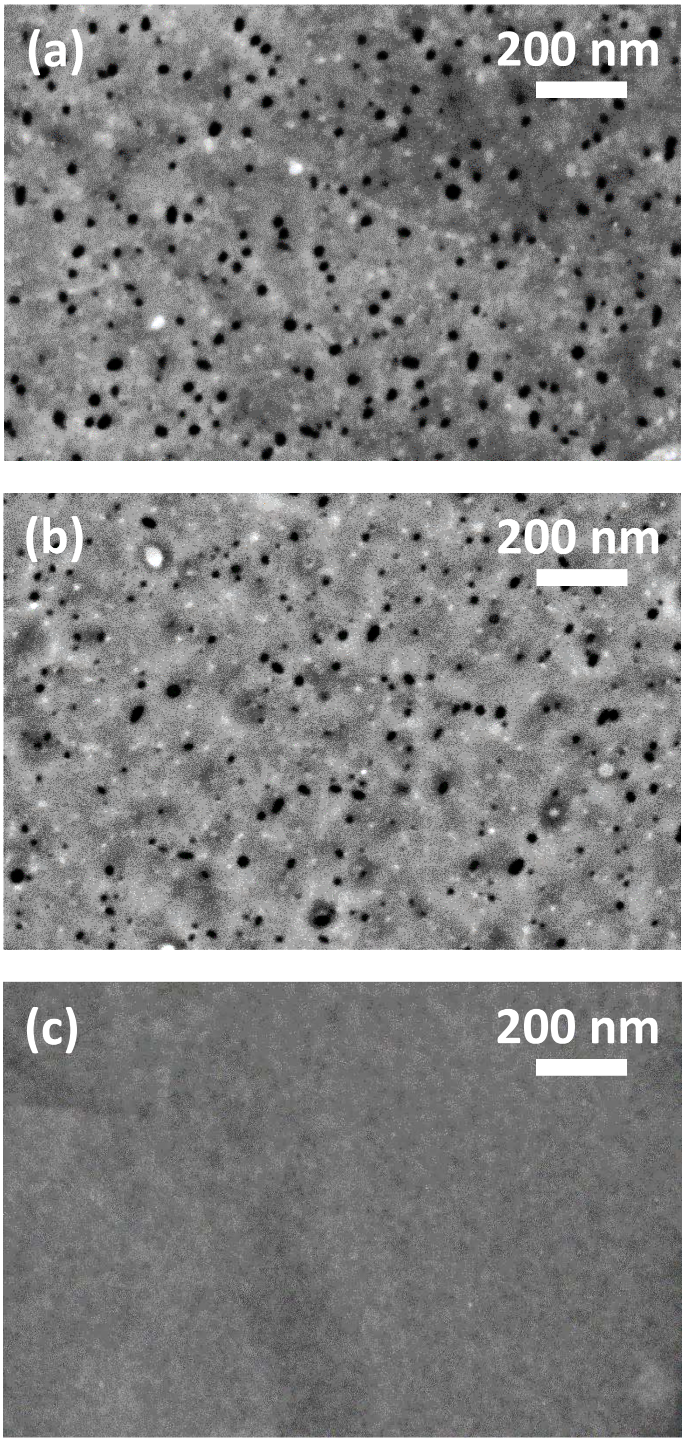

Figure 4: High resolution SEM observations at 5 kV of (a): wrought 17-4 PH steel aged 4 hours at 580°C, (b) SLM-ed steel aged 4 hours at 580°C, (c) wrought 17-4PH steel in the quenched state, used here as a control specimen without precipitation.

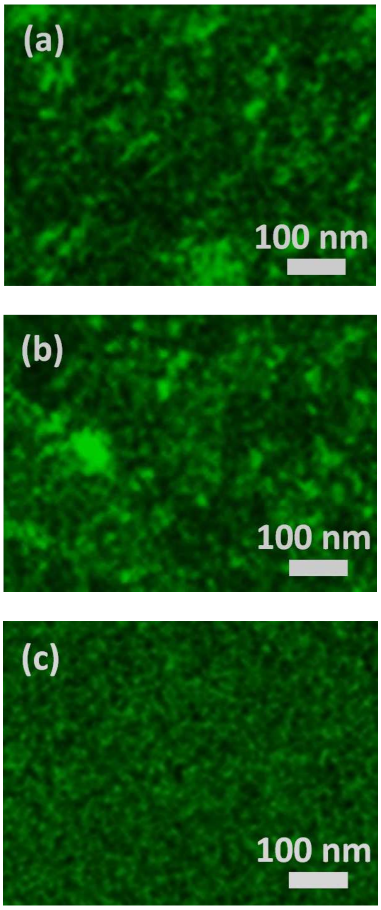

Figure 5: High resolution EDX maps acquired at 5 kV of (a): wrought 17-4 PH steel aged 4 hours at 580°C, (b) SLM-ed steel aged 4 hours at 580°C, (c) wrought 17-4PH steel in the quenched state, used here as a control specimen without precipitation. Lighter green indicates higher copper concentration.

Tensile properties in air

Tensile tests in air were performed at room temperature on both smooth and notched specimens of wrought and SLM-ed steels aged 4 hours at 580°C. It should be reminded that for the SLM-ed steel, the tensile direction corresponds to X direction in Figure 2. Figure 6 shows the engineering stress-strain curves obtained. The engineering stress was calculated from the ratio of load to minimum cross-section perpendicular to the load axis. For the smooth specimens, both wrought and SLM-ed steels show a significant elongation (21 to 26 %). It is remarkable that the strength of the ferritic SLM-ed material is only about 100 MPa below that of the wrought martensitic material. The strength of martensitic steels has been the subject of many research works (see for example the review paper by Krauss [36]). Considering the possible strengthening mechanisms, the yield strength σ_y can be described by the following equation [27]:

$$\sigma_y = \sigma_0 + \sigma_{ss} + \sigma_p + M\alpha\mu b\sqrt{\rho} + k_{HP}d^{-1/2} \qquad 2)$$

where σ_0 is the friction stress for pure iron, σ_{ss} is the solid solution strengthening, σ_p is the precipitation strengthening, M is the Taylor factor, α is the forest dislocation strengthening factor, μ is the shear modulus, b is the Bürgers vector, ρ is the dislocation density, k_{HP} is the Hall-Petch constant and d is the grain size. It was shown in a previous work using neutron diffraction that the dislocation density in the wrought 17-4PH steel is very high, i.e. of the order of 10^{15} m^{-2}, in the quenched state [31]. To our knowledge, no measurement of dislocation density in 17-4PH steel obtained from SLM has been reported in literature. However, values as high as 10^{15} m^{-2} have been reported for 316 SLM-ed stainless steel in the as-fabricated state [37]. It is reasonable to assume a dislocation density of the same order in the SLM-ed 17-4PH in the as-fabricated state. However, it has been shown that dislocation density in 17-4PH steel is significantly decreased when the material is aged above 500°C. Christien et al. [31] have shown that it is decreased by a factor of 10 after some minutes of isothermal annealing at 600°C. So it is reasonable to assume that the dislocation density is not higher than 10^{14} m^{-2} in the two materials studied here (wrought and SLM-ed steels aged 4 hours at 580°C). This would contribute to the yield strength by approximately 200 MPa if one considers $M\alpha\mu b \approx 20$ N m^{-1} in Eq. 2). This suggests that dislocation strengthening is not the main contribution to the yield strength in the materials studied here (1080 MPa and 980 MPa respectively in the wrought and SLM-ed aged 4 hours at 580°C, see Figure 6). As the two materials have the same crystal structure and very close compositions, the friction and solid solution terms σ_0 and σ_{ss} in Eq. 2) can be considered similar. In addition, if we assume that the contribution of copper precipitation hardening is the same, this would mean the 100 MPa difference in strength between the two materials would be due to the difference in grain size. Following Morito et al. [27], for a martensitic steel, the correct grain size to be considered in Eq. 2) is the block size, i.e. 3 µm for the wrought steel studied here. The Hall-Petch constant can then be estimated from Eq. 3):

$$k_{HP} = \frac{\Delta\sigma}{d_1^{-1/2} - d_2^{-1/2}} \qquad 3)$$

where $\Delta\sigma$ = 100 MPa, d_1 = 3 µm (block size in the wrought steel), d_2 = 20 µm (grain size in the SLM-ed steel). This gives k_{HP} = 283 MPa µm$^{1/2}$, which is in reasonable agreement with other values for α iron [38] (k_{HP} is strongly composition-dependent and values are in typically the range 100 to 700 MPa µm$^{1/2}$ for steels [38]). Considering the k_{HP} obtained, the grain boundary strengthening contribution can then be estimated to be about 160 MPa and 60 MPa for the wrought and SLM-ed material respectively. This suggests that the main contribution to the yield strength comes from the other terms of Eq. 2), i.e. the sum of friction (σ_0), solid solution (σ_{ss}) and precipitation hardening (σ_p). This can be estimated by subtracting the dislocation and grain boundary strengthening contributions from the experimental yield strength, which gives approximately $\sigma_0 + \sigma_{ss} + \sigma_p$ = 720 MPa.

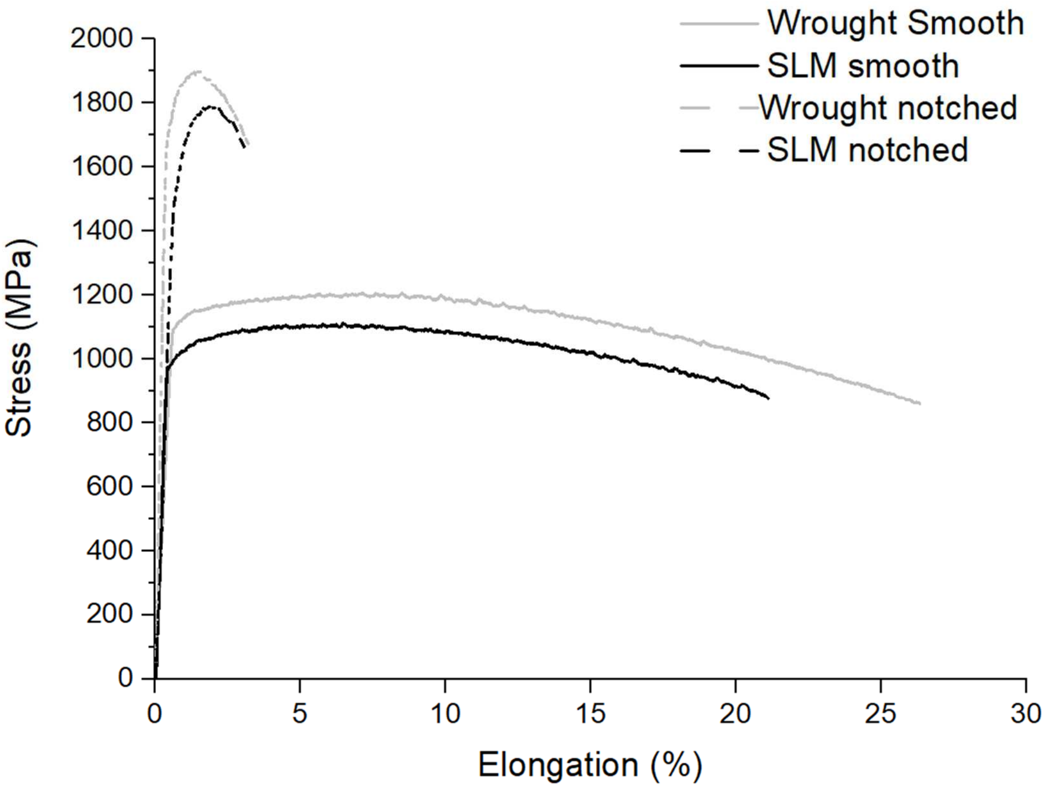

Figure 6: Stress-strain curves of tensile tests in air of smooth and notched specimens of wrought and SLM-ed steels. The displacement rate is 10^{-5} mm/s. Both steels are aged 4 hours at 580°C.

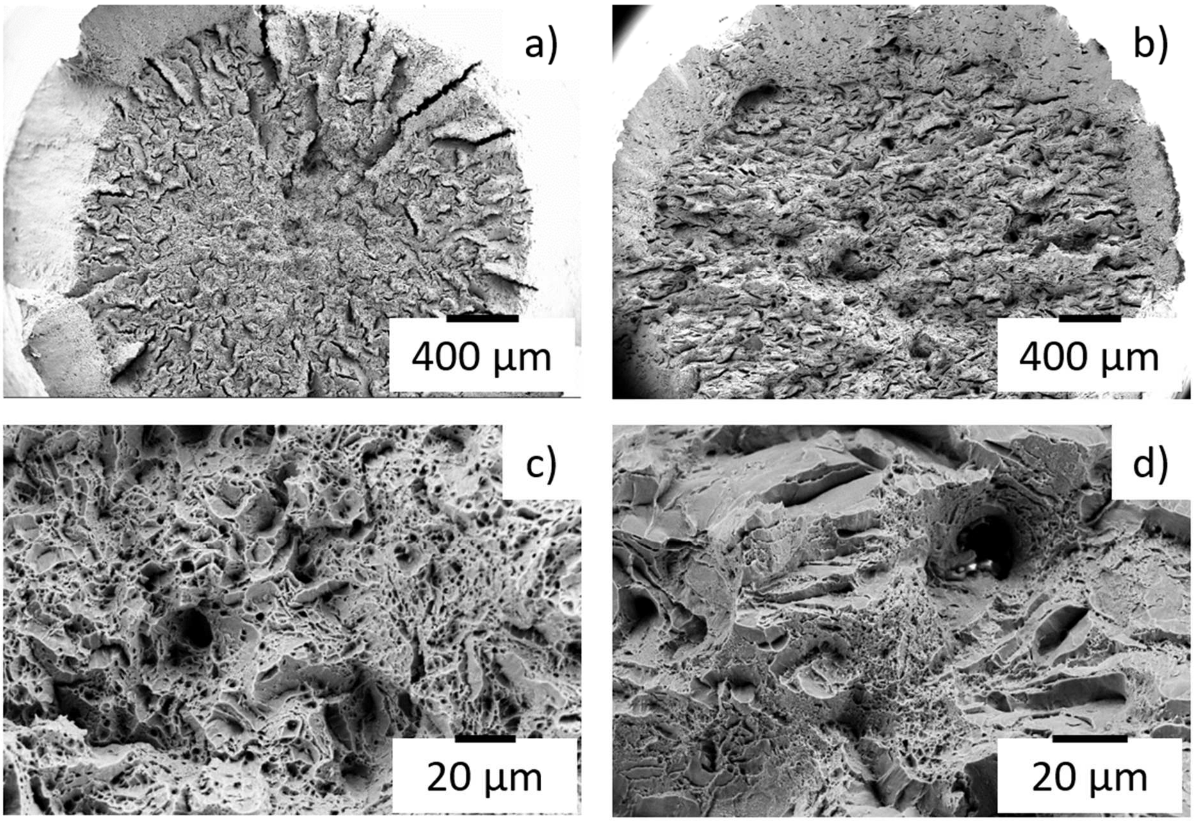

Figure 7: Fracture surfaces after tensile tests in air of smooth specimens of: (a), (c) wrought steel showing a typical ductile cup-and-cone fracture and (b), (d) SLM-ed steel showing ductile behavior with small brittle cleavage zones. Both steels are aged 4 hours at 580°C.

The notched specimens showed a pronounced increase in the engineering tensile stress and reduction in elongation compared to the smooth specimens. This was observed for both wrought and SLM-ed specimens and results from the stress triaxiality that develops ahead of the notch. In addition, the SLM-ed specimen had slightly lower notched nominal yield strength and notched nominal ultimate tensile strength than the wrought specimen, which is consistent with the observations on the smooth specimens.

Figure 7 shows the fracture surfaces of the wrought and SLM-ed steels obtained on smooth tensile specimens. Dimples were observed on the whole area of the fracture surface, which are typical of ductile failure. The two steels show a typical ductile cup-and-cone fracture. The shear lips are clearly visible on the edge. The fracture surfaces of the notched specimens are shown in Figure 8. The macroscopic fracture surface of the notched wrought steel, shown in Figure 8a, reveals a ductile fracture. At higher magnification (Figure 8c), the central zone is mainly (80%) ductile, but some brittle regions (20%) can be observed. The brittle facets show no river patterns and their size is about $\sim$ 10 to 20 µm, which suggests that they are intergranular facets, i.e. along prior austenitic grain boundaries. Similar intergranular facets were observed on the same 17-4PH material in [39] in mixed ductile/intergranular fracture surfaces obtained at different temperatures. The overall fracture surface of the SLM-ed notched steel in Figure 8b does not show a ductile fracture mode. The shear lips are much less pronounced than for the wrought material. In addition, at higher magnification (Figure 8d), mainly brittle transgranular cleavage is observed. It appears that the notch had a drastic effect on the fracture mode for the ferritic SLM-ed steel. It is well known that the notch introduces stress triaxiality that makes plastic deformation more difficult and promotes brittle behavior of the material. Figure 8c and Figure 8d indicate that the brittle regions observed on the fracture surfaces correspond to transgranular cleavage on the SLM-ed material, but intergranular fracture on the wrought material. This suggests that in the SLM-ed material, the transgranular cleavage stress is below the intergranular fracture stress, whereas it is the reverse in the wrought steel.

It is well known that cleavage fracture occurs in three stages: initiation of a crack due to dislocation pile-up on a grain boundary or particle, initial extension of the nucleated crack until the first obstacle, and the propagation beyond this obstacle, usually a grain boundary [40] [41]. These mechanisms were recently reviewed by Pineau et al. [42]. The theory developed by Smith [43] for the "formation of a cleavage crack in a crystalline solid" shows that, except for extremely brittle materials and/or at very low temperature, the "critical event", i.e. the one associated with the highest stress, is not initiation, but initial extension or propagation. Anyhow the stress needed to overcome each stage is inversely proportional to the square root of the grain size *d*. Thus, whatever the critical stage is, the cleavage fracture stress σ_f is inversely proportional to the square root of the grain size ($\sigma_f \propto d^{-1/2}$) [44]. This was demonstrated in early works in the frame of the dislocation theory of fracture [45–48]. Considering the two steels studied here, the martensitic block size for the wrought steel is about 3 µm, which is much smaller than the δ grain size for the SLM-ed steel (~20 µm). Thus, the transgranular cleavage stress σ_f is lower for the SLM-ed steel than for the wrought steel by a factor of $\sqrt{20/3} \approx 2.5$. This implies that transgranular cleavage is much easier in the SLM-ed ferritic steel than in the martensitic wrought steel. This is in agreement with the absence of transgranular cleavage observed in the martensitic wrought steel (Figure 8c).

In the case of an intergranular fracture, the three stage concept (nucleation, initial extension, propagation) is similar as for transgranular cleavage. In most cases however, the brittle fracture of BCC metals is obtained by transgranular cleavage, rather than intergranular fracture. This indicates that grain boundary fracture is usually a more difficult process than transgranular cleavage. Guttmann has suggested that this may be due to the high bifurcation angle of the crack at the triple junctions [49]. For a martensitic steel, the relevant grain size to be considered is not the same depending on whether the fracture is obtained from transgranular cleavage or intergranular fracture. In the case of transgranular cleavage, the relevant grain size is the martensite block size (~3 µm), whereas for intergranular fracture along prior austenitic grain boundary, the prior austenitic grain size (~10 µm) should be considered. This implies that in martensitic materials, the intergranular fracture may be facilitated with respect to transgranular cleavage, compared to non-martensitic materials. This could explain why in the notched tensile specimens illustrated in Figure 8, the brittle regions correspond to cleavage in the ferritic material and to intergranular fracture in the martensitic one.

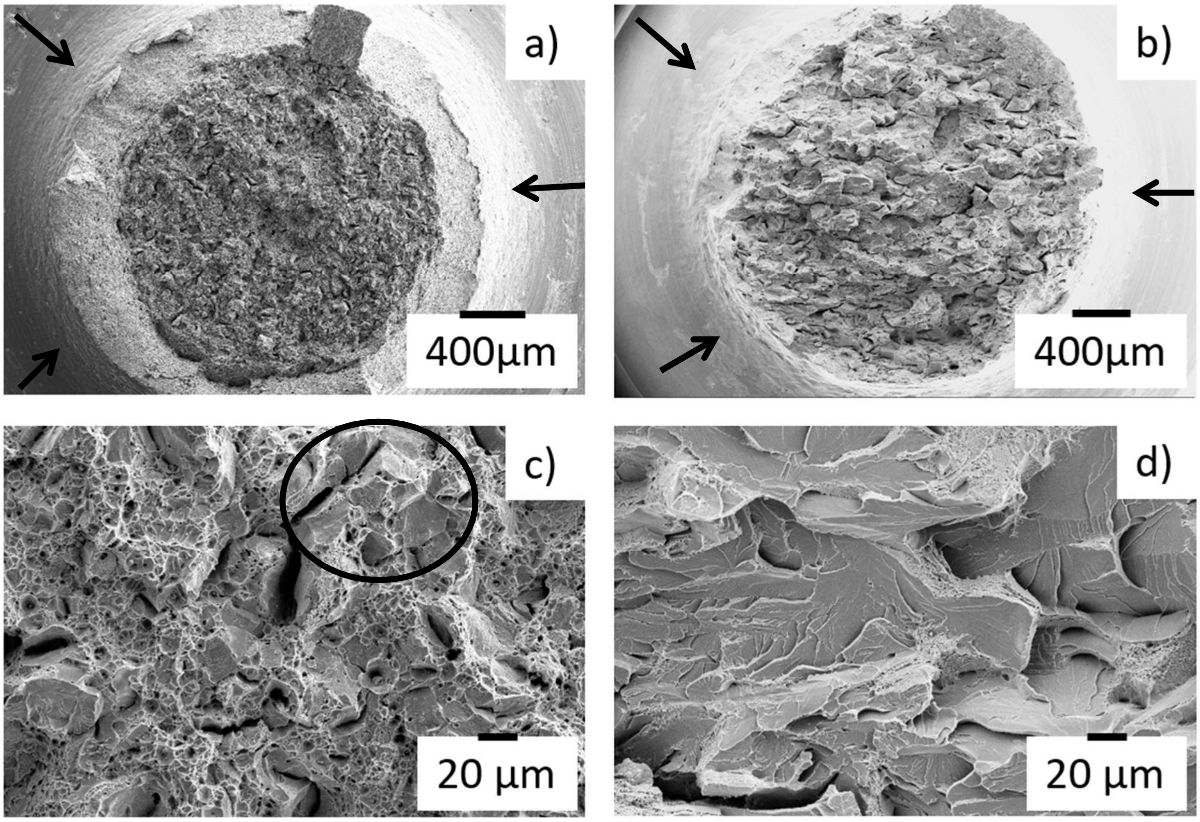

Figure 8: Fracture surfaces after tensile tests in air of notched specimens of: (a), (c) wrought steel showing mainly ductile behavior and some intergranular facets (circled area for example) and (b), (d) SLM-ed steel showing brittle behavior with cleavage. The arrows indicate the location of the notch. Both steels are aged 4 hours at 580°C.

Hydrogen permeation behavior

The permeation tests were conducted in order to study the hydrogen diffusion in the two steels. Figure 9 shows the hydrogen permeation curves of the wrought steel along an arbitrary direction and SLM-ed steel along two directions, parallel and perpendicular to the building direction Z. During tensile tests under hydrogen charging of cylindrical specimens, hydrogen charging occurs along multiple directions. For the wrought steel, the microstructure, and hence, the hydrogen diffusion is isotropic, i.e. the same for all directions. Thus, one permeation test is enough to determine the hydrogen diffusion of this steel. However, for the SLM-ed steel, Figure 2b and Figure 2d show that the microstructure is not isotropic. According to the literature, the hydrogen diffusion might differ for the same steel with changes of microstructure such as grain shape and size [50–52]. Therefore, two directions were studied to check if the hydrogen diffusion is anisotropic. In Figure 9, the normalized current density is plotted as a function of the normalized time. All the curves consisted of three stages: incubation stage preceding the breakthrough time, which corresponds to the time needed for the first hydrogen atoms to diffuse across the specimen's thickness, the transient stage where the permeation current increases and the steady-state stage where a constant hydrogen flux is reached. From these curves, the effective hydrogen diffusion coefficient can be calculated using the time lag method as explained previously. The results are listed in Table 2. The diffusion coefficient was similar for the two directions of the SLM-ed steel. Thus, it can be considered that the hydrogen diffusion in the SLM-ed steel is only slightly anisotropic. On the other hand, the hydrogen diffusion coefficient is about three times lower in the wrought steel than in the SLM-ed steel. This might be correlated to the higher grain boundary density in the martensitic microstructure, as it is known that grain boundaries can be trapping sites for hydrogen [53]. However, it should be noted that the diffusion coefficient found for the ferritic SLM-ed steel is approximately two to three orders of magnitude lower than that of a typical ferritic microstructure [54–56]. This could be due to additional trapping sites, possibly correlated to the formation of Cu-rich precipitates during ageing (4 hours at 580°C).

By using the effective diffusion coefficient calculated from the permeation tests, it is possible to estimate the hydrogen diffusion distance x from the surface of the charged tensile specimens according to the equation $x = \sqrt{2Dt}$ (although it should be mentioned that this gives only a rough estimation as stress effects are neglected). The value of t corresponds to the test duration from the onset of charging up to the specimen's fracture, which includes the possible 24 hours of pre-charging. Among all the conditions investigated in this study, the highest diffusion distance obtained was 500 µm (for the H pre+charged SLM-ed steel tested at 10^{-5} mm/s). This simple calculation shows that the H diffusion distance over the tensile testing time (including pre-charging) is much shorter than the specimen radius in any of the conditions investigated in this work.

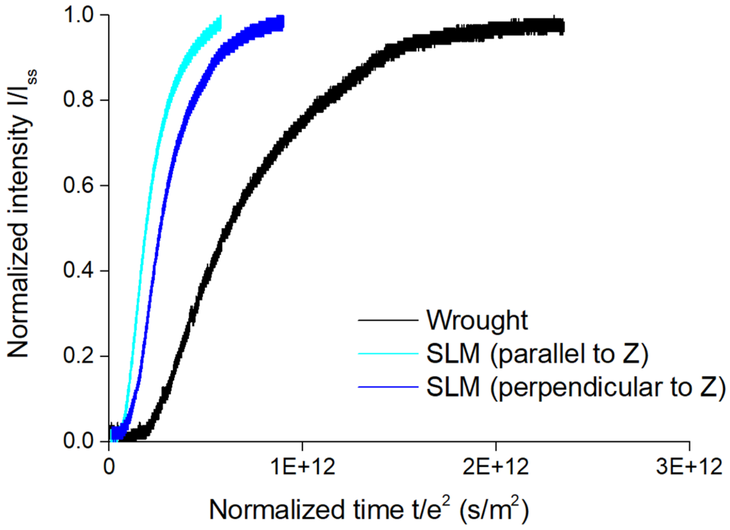

Figure 9: Electrochemical hydrogen permeation curves at room temperature of the wrought and SLM-ed steels aged 4 hours at 580°C.

Table 2: The effective diffusion coefficients of hydrogen in wrought and SLM-ed steels aged 4 hours at 580°C determined from electrochemical permeation at room temperature using the 63% time lag method.

Materials	D_{eff} ($m^2 s^{-1}$)
Wrought	$2.3\ 10^{-13}$
SLM (parallel to Z)	$7.3\ 10^{-13}$
SLM (perpendicular to Z)	$5.1\ 10^{-13}$

Tensile tests under hydrogen charging

It is reminded that only smooth specimens were tested under hydrogen charging. The tensile stress-strain curves obtained for the smooth specimens of both wrought and SLM-ed steels under hydrogen charging are given in Figure 10 and Figure 11. In order to compare the hydrogen susceptibility of each steel, the tensile stress-strain curves in air of smooth specimens were added to the figures. Different parameters (elongation to fracture, reduction in area and maximum stress) are summarized in Table 3. A pronounced effect of hydrogen charging can be observed for the two steels. For the SLM-ed steel (Figure 11), this effect is characterized by a strong reduction in elongation to fracture and in maximum stress. For the wrought steel, a reduction in elongation is observed, but the maximum stress is not strongly affected.

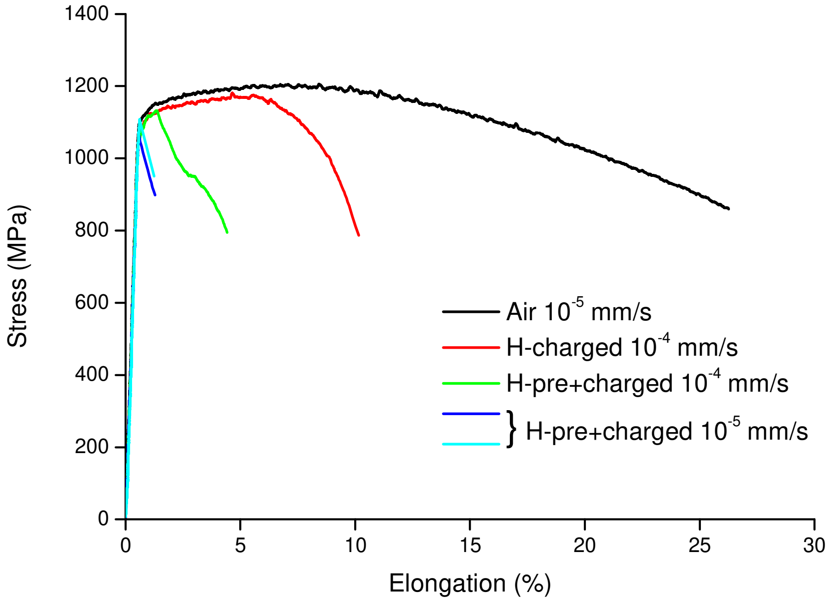

Figure 10: Stress-strain curves of wrought smooth specimens (aged 4 hours at 580°C) tested in air and under hydrogen charging at different displacement rates, with or without 24 h of H pre-charging.

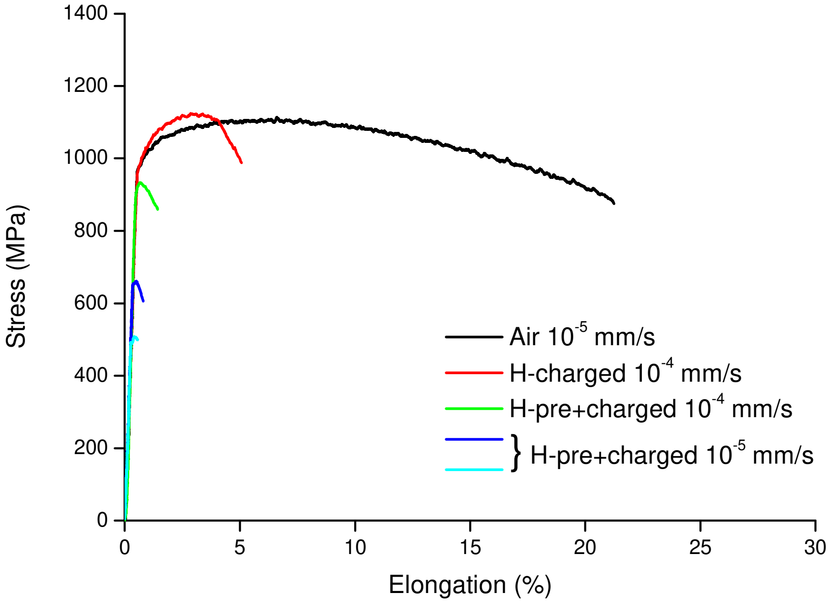

Figure 11: Stress-strain curves of SLM-ed smooth specimens (aged 4 hours at 580°C) tested in air and under hydrogen charging at different displacement rates, with or without 24 h of H pre-charging.

Table 3: Mechanical properties extracted from Figure 10 and Figure 11 for the wrought and SLM-ed steels aged 4 hours at 580°C and tensile tested under air and hydrogen cathodic charging. The reduction in area was measured after fracture in the necking region, if any. (1): mean values from the two tests conducted.

		Air	H cathodic charging		
				24 h of pre-charging	
Displacement rate (mm/s)		10^{-5}	10^{-4}	10^{-4}	10^{-5} (1)
Elongation to fracture (%)	Wrought	25.9	9.8	4.1	0.8
	SLM-ed	*20.8*	*4.6*	*1.0*	*0.4*
Reduction in area (%)	Wrought	32	~ 0	~ 0	~ 0
	SLM-ed	*24*	*~ 0*	*~ 0*	*~ 0*
Max. stress (MPa)	Wrought	1200	1170	1130	1060
	SLM-ed	*1110*	*1120*	*930*	*580*

Subcritical crack growth

Figure 12 shows a side view of wrought and SLM-ed H-charged specimens tested at 10^{-4} mm/s. Both specimens show a considerable number of small secondary cracks that initiated and slightly propagated but did not induce the final fracture. The direction of propagation is perpendicular to the tensile axis. These cracks present evidence of subcritical crack growth occurring in the two steels. Thus, the fracture in the two steels can be described by these successive steps: subcritical multi-cracking, then the coalescence of some of them to form the main crack that propagates up to a critical length, and then the final fast overload fracture of the remaining ligament. Stress-strain curves under hydrogen charging in Figure 10 and Figure 11 also show evidence of subcritical crack growth. As presented in Table 3, necking is observed only under air. In contrast, no necking (i.e. no reduction in area) is observed under cathodic charging, although a decrease in load is observed on the tensile curves. This load drop under cathodic charging can be attributed to the propagation and coalescence of cracks, which decrease the rigidity of the specimen to such an extent that a load drop is obtained. In addition, it is observed that the load drop under cathodic charging occurs earlier than under air. This means that crack propagation and coalescence occurs before the onset of necking, which is consistent with the absence of reduction in area observed under cathodic charging. Similar behavior was observed in hot cracking in austenitic alloys due to impurity sulphur [57].

The gradual decreases in load observed in Figure 10 and Figure 11 are very slow: they correspond to durations ranging from 20 minutes to 10 hours depending on the testing conditions. This shows that the cracks propagate slowly across the specimen, i.e. subcritically. This implies that hydrogen has sufficient time to interact with the crack tip and induce a hydrogen-assisted cracking phenomenon. On the other hand, the final overload fracture of the remaining ligament occurs critically, i.e. at very high speed (of the order of the speed of sound), which prevents any crack/hydrogen dynamic interaction.

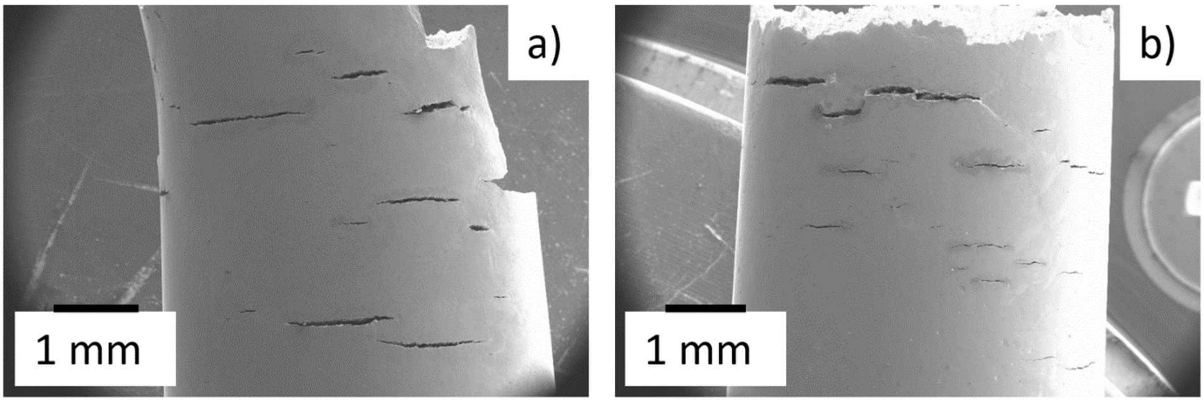

Figure 12: Secondary cracks in charged specimens at 10^{-4} mm/s. (a) wrought steel. (b): SLM-ed steel. Both steels are aged 4 hours at 580°C.

The fracture surface of the H-pre+charged wrought specimen at 10^{-4} mm/s displacement rate is given in Figure 13a and Figure 13c. It is also representative of the fracture surface of the other wrought specimens tested in different conditions. The overall surface is essentially composed of two different zones: a brittle zone located close to the surface and a ductile zone with dimples located in the center. The brittle zone is intergranular, i.e. along the prior austenitic grain boundaries. Subcritical cracking initiates at the surface and propagates into the specimen. It is then inferred that the intergranular brittle zone observed on the fracture surfaces corresponds to the subcritically propagated crack. It should be noticed that the intergranular crack depth (~900 µm) observed here is significantly larger than the hydrogen diffusion distance which is 220 µm in the particular case of the specimen shown in Figure 13a and Figure 13c. This observation further supports the assumption of subcritical propagation, in which the crack tip is dynamically embrittled by hydrogen and can thus propagate on "long" distances even with limited hydrogen diffusion [58–60]. Once the intergranular crack has propagated to a certain distance, overload fracture occurs, which corresponds to the central zone of the fracture surface shown in Figure 13a. This zone is ductile, which is consistent with the fracture mode observed for this material on smooth and notched specimens under air (Figure 7a, Figure 7c, Figure 8a and Figure 8c).

The fracture surface of the H-pre+charged SLM-ed specimen tested at 10^{-4} mm/s displacement rate is given in Figure 13b and Figure 13d. It is also similar to the fracture surfaces of the other SLM-ed specimens tested in different conditions. Unlike the wrought steel, the overall surface shows a brittle aspect. At higher magnification, the whole surface exhibits transgranular cleavage. Multiple cracking observed in Figure 12b, as well as the load drop observed in Figure 11, together with the absence of necking, show that subcritical crack growth is significant in the SLM-ed steel as well. Fracture surfaces presented in Figure 13b and Figure 13d show that both subcritical and critical crack propagation are obtained by transgranular cleavage. Thus they cannot be distinguished on the fracture surface. The observation that overload fracture is obtained by transgranular cleavage is consistent with the same fracture mode observed under air on a notched specimen of the SLM-ed material (Figure 8b and Figure 8d). Under hydrogen charging, the subcritically propagated crack behaves as a severe notch which promotes a brittle overload fracture by transgranular cleavage.

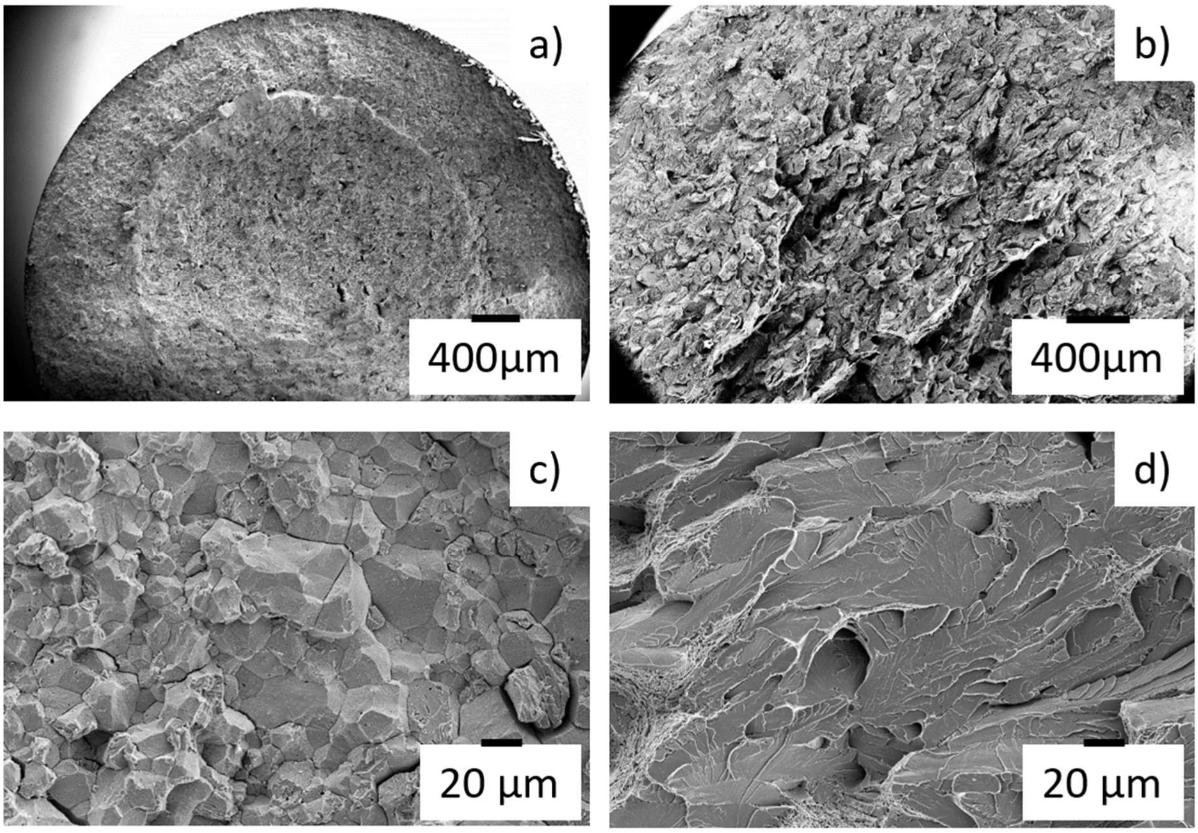

Figure 13: Fracture surfaces after tensile test at 10^{-4} mm/s under hydrogen charging of smooth specimens of (a), (c) wrought steel showing intergranular fracture close to the specimen surface and (b), (d) SLM-ed steel showing transgranular cleavage on the entire surface.

Effect of grain size

Figure 10, Figure 11 and Table 3 show that the reduction in elongation and maximum stress are more pronounced for the SLM-ed steel than for the wrought one. Thus it can be concluded that the ferritic SLM-ed steel is more susceptible to hydrogen embrittlement than the martensitic wrought steel, although its yield strength is slightly lower. This can be attributed to differences in microstructure. As mentioned earlier, the stress needed to trigger crack initiation, initial extension and propagation beyond the first obstacle is inversely proportional to the square root of grain size. Thus, since the ferritic SLM-ed steel has higher grain size, the hydrogen-assisted crack initiation and propagation is easier in this steel than in the martensitic wrought steel. The specimens of SLM-ed steel pre-charged for 24 hours and tensile tested at 10^{-5} mm/s, fail in the elastic domain, which can be attributed to very early initiation and propagation of subcritical cracks.

The difference in subcritical cracking path in the two materials is noticeable: it is entirely intergranular (along prior austenitic grain boundaries) in the wrought material, whereas it is transgranular in the SLM-ed material. A possible explanation relies on the martensitic microstructure itself. As martensite block size is very small (3 µm), in the case of a transgranular crack, cracking path would be relatively tortuous, with frequent bifurcations, which would make the propagation difficult. In contrast, as the prior austenitic grain size is higher (~10 µm), intergranular cracking path is less tortuous. This would make intergranular cracking easier than transgranular cleavage in the wrought martensitic steel. It should be noticed that the same tendency is observed when the material is tested under air. It is observed in Figure 8 that when the fracture (here overload) becomes partly brittle (in this case because of the stress triaxiality), the brittle facets correspond to transgranular cleavage in the ferritic SLM-ed steel (Figure 8d), whereas they are intergranular (along prior austenitic grain boundaries) in the martensitic wrought steel (Figure 8c). This confirms the higher intrinsic propensity of the martensitic microstructure to intergranular fracture (along prior austenitic grain boundaries), rather than transgranular cleavage.

Effect of H pre-charging and displacement rate

The comparison of the specimen tensile tested at 10^{-4} mm/s with and without H pre-charging (green and red curves in Figure 10 and Figure 11) shows a significant effect of 24 hours of pre-charging. This shows that subcritical cracks initiate and propagate easier in the pre-charged specimens. Considering an average H diffusion coefficient of $5\ 10^{-13}$ $m^2\ s^{-1}$ in the two materials, 24 hours of pre-charging give a diffusion distance into the material of approximately 300 µm, which is above the grain size of any of the materials. As mentioned earlier in this paper, the three steps of brittle fracture (initiation, initial extension and propagation beyond the first obstacle) involve distances of the order of the grain size. If, before starting mechanical loading, hydrogen is already accumulated below the surface on a distance larger than the grain size, which is the case here, subcritical crack initiation and propagation will be facilitated.

The comparison of the specimens tensile tested at 10^{-4} mm/s and 10^{-5} mm/s (with H pre-charging, green and blue curves in Figure 10 and Figure 11) shows that the materials are more susceptible to H cracking if the displacement rate is decreased. This could result from an effect of displacement rate on initiation and/or propagation. If the displacement rate is decreased, more time is allowed for (1) H accumulation below the surface, which will facilitate crack initiation, and (2) dynamic interactions at the crack tip, once it is initiated, which will facilitate crack propagation.

Conclusion

In this work, the microstructure and resistance to hydrogen embrittlement of wrought and SLM-ed 17-4PH steels were studied. The main conclusions about microstructure can be summarized as follows:

1. The wrought steel showed a typical martensitic microstructure with lathes. However, the SLM-ed steel exhibited a δ-ferritic microstructure with relatively coarse grains. This was due to the high cooling and heating rates experienced during SLM that suppressed the austenite formation and retained the δ ferrite down to room temperature.
2. After ageing 4 hours at 580°C, both wrought and SLM-ed steels showed nanoscale copper precipitation.

The hydrogen embrittlement was studied using slow strain rate tensile tests in acidic chloride medium at room temperature under cathodic charging. The same ageing treatment (4 hours at 580°C) was conducted on the two steels (wrought and SLM as-built). The degree of hydrogen susceptibility of each steel was assessed by comparing the stress-strain curves of uncharged, charged and pre+charged smooth specimens. The main conclusions that can be drawn are:

1. Tensile tests conducted in air showed that the ferritic SLM-ed steel has a yield strength only slightly lower than the martensitic wrought steel. The contributions of the different possible strengthening mechanisms were estimated in both materials.
2. Wrought and SLM-ed steels were both susceptible to hydrogen embrittlement under slow displacement rates. They exhibited a remarkable decrease in elongation to fracture compared with the uncharged steels.

3. The SLM-ed steel was more susceptible to hydrogen embrittlement than the wrought steel. This was attributed to the difference in grain size: the crack initiation and propagation was easier in the ferritic SLM-ed steel than in the martensitic wrought steel.
4. The fracture in both steels was obtained by subcritical cracking up to a critical length and then final fast overload fracture.
5. The fracture surface of the wrought steel showed two zones: an intergranular brittle fracture zone close to the surface and a ductile zone in the center. The intergranular fracture zone corresponds to the subcritical crack propagation. The ductile zone is correlated to the final fast overload fracture, which is consistent with the fracture mode of wrought notched specimen tested in air.
6. On the other hand, in the SLM-ed steel, both the subcritical crack growth and the final fast overload fracture were obtained by transgranular cleavage. The overload fracture mode is consistent with the fracture mode of SLM-ed notched specimen tested in air.

Acknowledgments

Tuomo Nyyssönen at Tampere University of Technology is acknowledged for supplying the script for the austenite grain reconstruction. The authors would like to acknowledge financial support from Institut CARNOT M.I.N.E.S (project #60678) and from LABEX MANUTECH-SISE (ANR-10-LABX-0075) of Université de Lyon, within the program “Investissements d’Avenir” (ANR-11-IDEX-0007) operated by the French National Research Agency (ANR).

References

[1] J.C.M. Farrar, in: The Alloy Tree: A Guide to Low-Alloy Steels, Stainless Steels, and Nickel-Base Alloys, CRC Press ; Woodhead Pub, Boca Raton : Cambridge, Eng, 2004: pp. 44–45.
[2] C.N. Hsiao, C.S. Chiou, J.R. Yang, Aging reactions in a 17-4 PH stainless steel, Materials Chemistry and Physics. 74 (2002) 134–142. https://doi.org/10.1016/S0254-0584(01)00460-6.
[3] U.K. Viswanathan, S. Banerjee, R. Krishnan, Effects of aging on the microstructure of 17-4 PH stainless steel, Materials Science and Engineering: A. 104 (1988) 181–189. https://doi.org/10.1016/0025-5416(88)90420-X.

[4] W.D. Yoo, J.H. Lee, K.T. Youn, Y.M. Rhyim, Study on the Microstructure and Mechanical Properties of 17-4 PH Stainless Steel Depending on Heat Treatment and Aging Time, Solid State Phenomena. 118 (2006) 15–20. https://doi.org/10.4028/www.scientific.net/SSP.118.15.

[5] M. Murayama, K. Hono, Y. Katayama, Microstructural evolution in a 17-4 PH stainless steel after aging at 400 °C, Metallurgical and Materials Transactions A. 30 (1999) 345–353. https://doi.org/10.1007/s11661-999-0323-2.

[6] W.C. Chiang, C.C. Pu, B.L. Yu, J.K. Wu, Hydrogen susceptibility of 17-4 PH stainless steel, Materials Letters. 57 (2003) 2485–2488. https://doi.org/10.1016/S0167-577X(02)01298-3.

[7] Y. Hayashi, T. Ito, Y. Nishimura, K. Takai, The states of hydrogen and hydrogen embrittlement susceptibility of precipitation hardened SUS630 stainless steel, IOP Conf. Ser.: Mater. Sci. Eng. 461 (2018) 012023. https://doi.org/10.1088/1757-899X/461/1/012023.

[8] S. Shen, X. Li, P. Zhang, Y. Nan, G. Yang, X. Song, Effect of solution-treated temperature on hydrogen embrittlement of 17-4 PH stainless steel, Materials Science and Engineering: A. 703 (2017) 413–421. https://doi.org/10.1016/j.msea.2017.06.078.

[9] C.T. Murray, Hydrogen Embrittlement of 15-5 PH Stainless Steels, MTA. 12 (1981) 2138–2141. https://doi.org/10.1007/BF02644189.

[10] P.K. Gokuldoss, S. Kolla, J. Eckert, Additive Manufacturing Processes: Selective Laser Melting, Electron Beam Melting and Binder Jetting—Selection Guidelines, Materials. 10 (2017) 672. https://doi.org/10.3390/ma10060672.

[11] T.D. Ngo, A. Kashani, G. Imbalzano, K.T.Q. Nguyen, D. Hui, Additive manufacturing (3D printing): A review of materials, methods, applications and challenges, Composites Part B: Engineering. 143 (2018) 172–196. https://doi.org/10.1016/j.compositesb.2018.02.012.

[12] C.Y. Yap, C.K. Chua, Z.L. Dong, Z.H. Liu, D.Q. Zhang, L.E. Loh, S.L. Sing, Review of selective laser melting: Materials and applications, Applied Physics Reviews. 2 (2015) 041101. https://doi.org/10.1063/1.4935926.

[13] M. Rombouts, J.-P. Kruth, L. Froyen, P. Mercelis, Fundamentals of selective laser melting of alloyed steel powders, CIRP Annals-Manufacturing Technology. 55 (2006) 187–192. https://doi.org/10.1016/S0007-8506(07)60395-3.

[14] J.P. Kruth, L. Froyen, J. Van Vaerenbergh, P. Mercelis, M. Rombouts, B. Lauwers, Selective laser melting of iron-based powder, Journal of Materials Processing Technology. 149 (2004) 616–622. https://doi.org/10.1016/j.jmatprotec.2003.11.051.

[15] M. Alnajjar, F. Christien, K. Wolski, C. Bosch, Evidence of austenite by-passing in a stainless steel obtained from laser melting additive manufacturing, Additive Manufacturing. 25 (2019) 187–195. https://doi.org/10.1016/j.addma.2018.11.004.

[16] T. Niendorf, S. Leuders, A. Riemer, H.A. Richard, T. Tröster, D. Schwarze, Highly Anisotropic Steel Processed by Selective Laser Melting, Metallurgical and Materials Transactions B. 44 (2013) 794–796. https://doi.org/10.1007/s11663-013-9875-z.

[17] H.K. Rafi, D. Pal, N. Patil, T.L. Starr, B.E. Stucker, Microstructure and Mechanical Behavior of 17-4 Precipitation Hardenable Steel Processed by Selective Laser Melting, Journal of Materials Engineering and Performance. 23 (2014) 4421–4428. https://doi.org/10.1007/s11665-014-1226-y.

[18] F. Hengsbach, P. Koppa, K. Duschik, M.J. Holzweissig, M. Burns, J. Nellesen, W. Tillmann, T. Tröster, K.-P. Hoyer, M. Schaper, Duplex stainless steel fabricated by selective laser melting - Microstructural and mechanical properties, Materials & Design. 133 (2017) 136–142. https://doi.org/10.1016/j.matdes.2017.07.046.

[19] K. Saeidi, L. Kevetkova, F. Lofaj, Z. Shen, Novel ferritic stainless steel formed by laser melting from duplex stainless steel powder with advanced mechanical properties and high ductility, Materials Science and Engineering: A. 665 (2016) 59–65. https://doi.org/10.1016/j.msea.2016.04.027.

[20] S. Li, M. Liu, Y. Ren, Y. Wang, Hydrogen embrittlement behaviors of additive manufactured maraging steel investigated by in situ high-energy X-ray diffraction, Materials Science and Engineering: A. 766 (2019) 138341. https://doi.org/10.1016/j.msea.2019.138341.

[21] Y.J. Kwon, R. Casati, M. Coduri, M. Vedani, C.S. Lee, Hydrogen Embrittlement Behavior of 18Ni 300 Maraging Steel Produced by Selective Laser Melting, Materials (Basel). 12 (2019). https://doi.org/10.3390/ma12152360.

[22] C. Örnek, Additive manufacturing – a general corrosion perspective, Corrosion Engineering, Science and Technology. 53 (2018) 531–535. https://doi.org/10.1080/1478422X.2018.1511327.

[23] G. Chai, S. Ronneteg, U. Kivisäkk, R.L. Peng, S. Johansson, Mechanisms of Hydrogen Induced Stress Crack Initiation and Propagation in Super Duplex Stainless Steels, Steel Research International. 80 (2009) 482–487. https://doi.org/10.2374/SRI09SP042.

[24] F. Bachmann, R. Hielscher, H. Schaeben, Grain detection from 2d and 3d EBSD data—Specification of the MTEX algorithm, Ultramicroscopy. 111 (2011) 1720–1733. https://doi.org/10.1016/j.ultramic.2011.08.002.

[25] T. Nyyssönen, M. Isakov, P. Peura, V.-T. Kuokkala, Iterative Determination of the Orientation Relationship Between Austenite and Martensite from a Large Amount of Grain Pair Misorientations, Metall and Mat Trans A. 47 (2016) 2587–2590. https://doi.org/10.1007/s11661-016-3462-2.

[26] G. Kurdjumow, G. Sachs, Über den Mechanismus der Stahlhärtung, Z. Physik. 64 (1930) 325–343. https://doi.org/10.1007/BF01397346.

[27] S. Morito, H. Yoshida, T. Maki, X. Huang, Effect of block size on the strength of lath martensite in low carbon steels, Materials Science and Engineering: A. 438–440 (2006) 237–240. https://doi.org/10.1016/j.msea.2005.12.048.

[28] M.A.V. Devanathan, Z. Stachurski, The adsorption and diffusion of electrolytic hydrogen in palladium, Proc. R. Soc. Lond. A. 270 (1962) 90–102. https://doi.org/10.1098/rspa.1962.0205.

[29] P. Lacombe, B. Baroux, G. Béranger, L. Colombier, J. Hochmann, Les aciers inoxydables, Les Editions de Physique, Les Ulis, France, 1990.

[30] F. Christien, M.T.F. Telling, K.S. Knight, A comparison of dilatometry and in-situ neutron diffraction in tracking bulk phase transformations in a martensitic stainless steel, Materials Characterization. 82 (2013) 50–57. https://doi.org/10.1016/j.matchar.2013.05.002.

[31] F. Christien, M.T.F. Telling, K.S. Knight, Neutron diffraction in situ monitoring of the dislocation density during martensitic transformation in a stainless steel, Scripta Materialia. 68 (2013) 506–509. https://doi.org/10.1016/j.scriptamat.2012.11.031.

[32] S. Vunnam, Effect of powder chemical composition on the as-built microstructure of 17-4 PH stainless steel processed by selective laser melting, Additive Manufacturing. (2019) 12.

[33] E.A. Lass, F. Zhang, C.E. Campbell, Nitrogen Effects in Additively Manufactured Martensitic Stainless Steels: Conventional Thermal Processing and Comparison with Wrought, Metall and Mat Trans A. (2020). https://doi.org/10.1007/s11661-020-05703-6.

[34] O. Andreau, I. Koutiri, P. Peyre, J.-D. Penot, N. Saintier, E. Pessard, T. De Terris, C. Dupuy, T. Baudin, Texture control of 316L parts by modulation of the melt pool morphology in selective laser melting, Journal of Materials Processing Technology. 264 (2019) 21–31. https://doi.org/10.1016/j.jmatprotec.2018.08.049.

[35] G. Yeli, M.A. Auger, K. Wilford, G.D.W. Smith, P.A.J. Bagot, M.P. Moody, Sequential nucleation of phases in a 17-4PH steel: Microstructural characterisation and mechanical properties, Acta Materialia. 125 (2017) 38–49. https://doi.org/10.1016/j.actamat.2016.11.052.

[36] G. Krauss, Martensite in steel: strength and structure, Materials Science and Engineering: A. 273–275 (1999) 40–57. https://doi.org/10.1016/S0921-5093(99)00288-9.

[37] S. Gorsse, C. Hutchinson, M. Gouné, R. Banerjee, Additive manufacturing of metals: a brief review of the characteristic microstructures and properties of steels, Ti-6Al-4V and high-entropy alloys, Sci Technol Adv Mater. 18 (2017) 584–610. https://doi.org/10.1080/14686996.2017.1361305.

[38] S. Takaki, Review on the Hall-Petch Relation in Ferritic Steel, Materials Science Forum. (2010). https://doi.org/10.4028/www.scientific.net/MSF.654-656.11.

[39] F. Christien, R. Le Gall, G. Saindrenan, Synergetic effect of hardness and phosphorus grain-boundary segregation on the ductile-to-brittle transition temperature of 17-4 PH steel,

Metallurgical and Materials Transactions A (Physical Metallurgy and Materials Science). 34A (2003) 2483–91.

[40] K. Shibanuma, S. Aihara, K. Suzuki, Prediction model on cleavage fracture initiation in steels having ferrite–cementite microstructures – Part I: Model presentation, Engineering Fracture Mechanics. 151 (2016) 161–180. https://doi.org/10.1016/j.engfracmech.2015.03.048.

[41] C.J. McMahon, M. Cohen, Initiation of cleavage in polycrystalline iron, Acta Metallurgica. 13 (1965) 591–604. https://doi.org/10.1016/0001-6160(65)90121-5.

[42] A. Pineau, A.A. Benzerga, T. Pardoen, Failure of metals I: Brittle and ductile fracture, Acta Materialia. 107 (2016) 424–483. https://doi.org/10.1016/j.actamat.2015.12.034.

[43] E. Smith, The formation of a cleavage crack in a crystalline solid—I, Acta Metallurgica. 14 (1966) 985–989. https://doi.org/10.1016/0001-6160(66)90219-7.

[44] G.E. Dieter, in: Mechanical Metallurgy, McGraw-Hill Education, 1961: pp. 190–220.

[45] C. Zener, The micro-mechanism of fracture, in: Fracturing of Metals, American Society for Metals, Metals Park, Ohio, 1948.

[46] A.N. Stroh, The Formation of Cracks as a Result of Plastic Flow, Proceedings of the Royal Society of London. Series A, Mathematical and Physical Sciences. 223 (1954) 404–414.

[47] A.N. Stroh, CXI. Brittle fracture and yielding, The London, Edinburgh, and Dublin Philosophical Magazine and Journal of Science. 46 (1955) 968–972. https://doi.org/10.1080/14786440908520617.

[48] A.H. Cottrell, THEORY OF BRITTLE FRACTURE IN STEEL AND SIMILAR METALS, Trans. Met. Soc. AIME. Vol: 212 (1958). https://www.osti.gov/biblio/4347093 (accessed February 13, 2020).

[49] M. Guttmann, Fragilité de revenu et ségrégation intergranulaire de l'antimoine et du manganèse dans les aciers faiblement alliés à 2% de manganèse, Université de Pairs XI, 1974.

[50] A. Oudriss, J. Creus, J. Bouhattate, E. Conforto, C. Berziou, C. Savall, X. Feaugas, Grain size and grain-boundary effects on diffusion and trapping of hydrogen in pure nickel, Acta Materialia. 60 (2012) 6814–6828. https://doi.org/10.1016/j.actamat.2012.09.004.

[51] A.J. Haq, K. Muzaka, D.P. Dunne, A. Calka, E.V. Pereloma, Effect of microstructure and composition on hydrogen permeation in X70 pipeline steels, International Journal of Hydrogen Energy. 38 (2013) 2544–2556. https://doi.org/10.1016/j.ijhydene.2012.11.127.

[52] Y. Cao, H. Li, J.A. Szpunar, W.T. Shmayda, Anisotropic Hydrogen Permeation in Nano/Poly Crystalline-Nickel Membranes, MRS Proc. 752 (2002) AA12.4. https://doi.org/10.1557/PROC-752-AA12.4.

[53] S.L.I. Chan, Hydrogen trapping ability of steels with different microstructures, Journal of the Chinese Institute of Engineers. 22 (1999) 43–53. https://doi.org/10.1080/02533839.1999.9670440.

[54] C.H. Tseng, W.V. Wei, J.K. Wu, Electrochemical methods for studying hydrogen diffusivity, permeability, and solubility in AISI 420 and AISI 430 stainless steels, 5 (1989) 4.

[55] J. Svoboda, G. Mori, A. Prethaler, F.D. Fischer, Determination of trapping parameters and the chemical diffusion coefficient from hydrogen permeation experiments, Corrosion Science. 82 (2014) 93–100. https://doi.org/10.1016/j.corsci.2014.01.002.

[56] T. Si, Y. Liu, Q. Zhang, D. Liu, Y. Li, Effect of Microstructure on Hydrogen Permeation in EA4T and 30CrNiMoV12 Railway Axle Steels, Metals. 9 (2019) 164. https://doi.org/10.3390/met9020164.

[57] F. Christien, Role of Impurity Sulphur in the Ductility Trough of Austenitic Iron–Nickel Alloys, Materials. 13 (2020) 539. https://doi.org/10.3390/ma13030539.

[58] H.H. Johnson, A.R. Troiano, Crack Initiation in Hydrogenated Steel, Nature. 179 (1957) 777.

[59] A.R. Troiano, The Role of Hydrogen and Other Interstitials in the Mechanical Behavior of Metals: (1959 Edward De Mille Campbell Memorial Lecture), Metallogr. Microstruct. Anal. 5 (2016) 557–569. https://doi.org/10.1007/s13632-016-0319-4.

[60] E. Martínez-Pañeda, Z.D. Harris, S. Fuentes-Alonso, J.R. Scully, J.T. Burns, On the suitability of slow strain rate tensile testing for assessing hydrogen embrittlement susceptibility, Corrosion Science. 163 (2020) 108291. https://doi.org/10.1016/j.corsci.2019.108291.